Nanostructuring of dense SnO2 ceramics by Spark Plasma Sintering

Fabian Delorme, Raphaël Dujardin, F. Schoenstein, B. Pintault, P. Belleville, Cecile Autret, I. Monot-Laffez, Fabien Giovannelli

Nanostructuring of dense SnO_2 ceramics by Spark Plasma Sintering

Authors : F. DELORME[1*], R. DUJARDIN[1], F. SCHOENSTEIN[2], B. PINTAULT[3], P. BELLEVILLE[3], **C. AUTRET[1]**, I. MONOT-LAFFEZ[1], F. GIOVANNELLI[1]

[1] Université de Tours, CNRS, INSA CVL, GREMAN UMR 7347, IUT de Blois, 15 rue de la chocolaterie, CS 2903, F-41029 Blois Cedex, France.

[2] Université Paris 13, Sorbonne Paris Cite, Laboratoire des Sciences des Procédés et des Matériaux - LSPM, CNRS, UPR 3407, 99 avenue Jean Baptiste Clément, F-93430 Villetaneuse, France.

[3] CEA, DAM Le Ripault, F-37260 Monts, France.

[*] : corresponding author. Tel. : +33-2-54-55-21-20 ; Fax : +33-2-54-55-21-09 ; E-mail : fabiandelorme@yahoo.fr.

Abstract :

The spark plasma sintering (SPS) behaviour of pure SnO_2 has been studied. **Two different SnO_2 powders have been studied: a commercial 50-200 nm one and 4-6 nm nanoparticles obtained by precipitation**. It has demonstrated that it is not possible to keep pure SnO_2 above **1223 K** by SPS. Indeed, at **1248 K**, SnO appears whereas at higher temperatures, samples are composed by SnO_2 and metal Sn. Three different cycles have been

developed that allow achieving high densities (≥ 94 %). The study of the grain size shows that when the density increases the grain size increases to reach 60-70 nm for the high density samples. Therefore, SPS can be successfully used to produce dense nanostructured SnO_2 ceramics without any sintering agent. Nanostructuring is very efficient to lower thermal conductivity as values as low as 6.59 and 3.99 $W.m^{-1}.K^{-1}$ at 373 and 1000 K respectively, are measured in SPS nanostructured ceramics. Moreover, the transport properties of the dense ceramics are the best reported for undoped SnO_2.

Keywords : Tin oxide ; Spark Plasma Sintering ; Thermoelectric ; Nanostructuring ; Thermal conductivity

1. INTRODUCTION

SnO_2 exhibits a rutile-type structure (space group : $P4_2/mnm$, a = b = 4.7382 Å and c = 3.1871 Å, theoretical density = 6.994, PDF card 41-1445) [1]. It is an n-type semiconductor with a wide band gap of 3.6 eV [2]. It combines high electrical conductivity with high optical transparency in the visible range of the electromagnetic spectrum [3]. Therefore, it is used for numerous applications such as transparent conducting oxide [4, 5], solid state gas sensor [3, 6-8], electrode [9], catalyst material [10], photoluminescence [11], varistor [12, 13], thermoelectric material [14-16] or for photovoltaic devices [17].

It is well known that achieving high density SnO_2 ceramics by conventional sintering is not possible due to non-densifying mechanisms such as the transformation of SnO_2 into SnO and vaporization of tin monoxide which occurs at a high rate above **1373 K** or surface diffusion and evaporation-condensation [18, 19]. Therefore, to overcome such a difficulty, one route has been to add sintering agents into SnO_2, such as CoO, Co_3O_4, MnO_2, CuO, ZnO, Sb_2O_3, … [18, 20-24]. However, the sintering agent can also affect properties and especially transport properties that are very sensitive to small amounts of dopants in that kind of oxides [23, 25]. Another route was to use high pressure. For instance, Park et al. [26] have obtained more than 97 % dense undoped SnO_2 ceramics by hot isostatic pressing carried out under 150 MPa at **1673 K** for 12 hours. However, such high temperature and long treatments leads also to grain growth and are not therefore a suitable solution for nanostructuring.

Spark Plasma Sintering (SPS) is now a well-known technique to sinter, in a few minutes, dense ceramic bodies of oxide materials at low temperature [27-35]. Therefore, SPS appears as a suitable technique to avoid or limit grain growth during sintering [28].

Few controversial reports have been published on spark plasma sintering of undoped SnO_2. Park et al. [36] obtained dense ceramics (relative density > 95 %) from commercial and home-made SnO_2 nanopowders at **1323 K** under 37.5 MPa during 5 minutes under vacuum whereas at **1273 K** in the same conditions, the relative density is only circa 72 %. Li et al. [37] have studied various sintering parameters on commercial SnO_2 powders. At **1323 K** under 37 MPa during 5 minutes under vacuum, they similarly found a relative density above 95 %. However, in the same conditions but at **1273 K**, they already had a 95 % dense ceramic. They also reported that increasing the pressure (up to 40 MPa), or the heating rate (up to **200 K.min^{-1}**) leads to higher relative densities and that 3 minutes are enough to reach the plateau of highly dense materials.

Vo et al. [16] have reported a very different SPS cycle to sinter undoped SnO_2 ceramics with relative density higher than 95 %. The sintering temperature is lower **1223 K** and the pressure higher, 90 MPa during 5 minutes under an argon atmosphere. Moreover, they add first a dwell at **773 K** during 2 minutes to reach the pressure. However, as their aim is to study thermoelectric properties of tantalum-doped SnO_2 ceramics, they do not explain the reasons for such a cycle.

Therefore, as the final aim of this article is to reach nanostructured dense SnO_2 without sintering agent, the influence of spark plasma sintering cycle parameters on the density of undoped SnO_2 ceramics will be first investigated. Then, grain size evolution will also be characterized as well as electrical and thermal conductivities of ceramics.

2. MATERIALS AND METHODS

Two kinds of SnO_2 powders have been used for this study. The first one is from Aldrich (≥ 99.9 % purity, ≈ 325 mesh, **50-200 nm grain size**) and is similar to the commercial powder used by Park et al. [36], and the second one was nanopowder synthesized according to the process described by Dujardin et al. [38] **(figure 1)**. Briefly, it consists in precipitating SnO_2 nanoparticles (4-6 nm) from the dropwise addition of a 1 M NaOH aqueous solution into a 2 M $SnCl_4$ aqueous solution at **373 K** under reflux.

Sintering was performed by Spark Plasma Sintering (Syntex 515 S). The synthesised powders were placed in a 15 mm diameter graphite die (MERSEN - carbon grade 2333) in argon atmosphere. Samples were separated from punches and die by graphite foils. Several conditions have been tested, as detailed below. Note that for experiments with pressure higher than 100 MPa, high strength composite graphite dies were used (TOYO TANSO - carbon grade CX31V).

The obtained pellets were then polished to remove the graphite foils used during the SPS process and cut with a diamond wire saw as bars perpendicular to the pressure axis for electric properties measurements or thin 6 mm squares parallel to the pressure axis for thermal diffusivity measurements to prevent any orientation effect.

Thermoelectric properties of the sintered samples were determined from simultaneous measurement of resistivity and Seebeck coefficient in a ZEM-3 equipment (ULVAC Technologies) and thermal conductivity. Seebeck coefficient and electrical conductivity have been measured first from 323 to 1000 K. The thermal diffusivity was measured using the laser flash diffusivity technique (Netzsch LFA 457) from 373 to 1000 K in vacuum after graphite coating. The thermal diffusivity measurement of all specimens was carried out three times at

each temperature. The heat capacity of the materials was measured from 300 to 1000 K, with a heating rate of **20 K.min^{-1}** in platinum crucibles and in nitrogen atmosphere, using differential scanning calorimetry (Netzsch STA 449 F3 Jupiter).

Apparent density of the samples was calculated from the weight and dimensions of the bars cut from the pellets for ZEM-3 characterization and theoretical density [1].

Powder X-ray diffraction (XRD) patterns have been performed on a BRUKER D8 Advance θ/2θ diffractometer equipped with a Linxeye energy-dispersive one-dimensional detector, using Cu-K$_\alpha$ radiation and operating at 40 kV and 40 mA at room temperature. The scans have been recorded from 20 to 70°(2θ) with a step of 0.02° and a counting time of 0.5 s per step.

The scanning electron microscopy (SEM) observations have been performed using Tescan Mira 3 field emission microscope coupled with an Energy Dispersive Spectrometer (EDS Oxford INCA X-Act) without prior coating of the samples.

3. RESULTS AND DISCUSSION

As the first SnO_2 nanopowder used in this study is similar to the one used by Park et al. [36], their SPS conditions were tried first, i.e. **1323 K** under a pressure of 37.5 MPa during 5 minutes (heating and cooling rate of **100 K.min^{-1}**). At the end of the SPS cycle, small Sn beads appear on the top of the graphite die (figure 2). The XRD pattern measured on the pellet is shown in figure 3a) and also exhibits presence of metal Sn peaks. A cross section observed

by SEM shows that metal tin (data not shown) can be observed on the surface of the pellet as well as in the core. The formation of metal tin is probably related to the reaction of SnO_2 with graphite on the surface of the pellet. Moreover, it has already been noticed that graphite can diffuse within ceramics [39, 40]. Indeed, replacing the graphite foil between the die and the sample by boron nitride or alumina powder allows to reduce the Sn amount but it is still possible to find some metal tin in the core of pellets. Moreover, similar results have been obtained for higher pressure (100 MPa) and with the nanoparticles synthesized using Dujardin et al.'s route [38].

The influence of temperature decrease has been studied with the nanoparticles synthesized using Dujardin et al.'s route [38]. The applied pressure is 100 MPa and the temperature dwell duration is 5 minutes with heating and cooling rate of **100 K.min^{-1}**. PXRD patterns (figure 3b) show that at **1248 K**, the peaks relative to Sn metal have disappeared. However, the phase is not pure SnO_2 as some peak corresponding to SnO can be observed. At **1223 K**, only the peaks related to SnO_2 are present (figure 3c). This is the temperature used by Vo et al. [16]. Moreover, PXRD patterns also shows that when temperatures decrease, the peaks intensity decreases and the full-width half-maximum increases. According to SEM images (figure 4) no secondary phase was observed, confirming the XRD results. Moreover, a small porosity can be observed: this is consistent with a poor relative density of 76 %. On the contrary to the results presented by Vo et al. [16], the addition of a dwell at **773 K** during 2 minutes before reaching **1223 K** doesn't allow to achieve relative density higher than 95 %, but leads to unchanged density.

Therefore, the influence of the SPS parameters (pressure, duration of the high temperature dwell, heating/cooling rate), whereas the highest temperature remains constant (i.e. **1223 K**)

has been studied to reach higher densities. Figure 5 shows the influence of the duration of the high temperature dwell. It clearly appears that the density is not significantly improved even for long SPS experiments of 30 minutes. The best relative density achieved is 79 % for a 10 minutes dwell. Figure 6 shows the influence of the applied pressure: Density increases as pressure increases for low pressures (P < 100 MPa) but reach a plateau for higher values. The best density achieved is 81 % at 150 MPa. Figure 7 shows the influence of the heating/cooling rate: An optimum value clearly exists around **200 K.min^{-1}** that allows reaching relative densities as high as 87 %. This effect of high heating rate on sintering has now been largely demonstrated [41, 42] but the reason for an optimum value remains unclear.

Individually, each optimized parameter does not allow to reach samples with relative densities of 95 % or higher. Therefore, they have been combined **(Table 1)**. By combining the most influent heating/cooling rate and duration of the high temperature dwell, the following SPS cycle (**Cycle A: 1223 K**-100 MPa-10 min-**200K.min^{-1}**) allows achieving 95 % relative density. One of the main interests of this sintering cycle is that working at a limited pressure, it is possible to use conventional graphite dies. Combining pressure and duration of the high temperature dwell, the following SPS cycle (**Cycle B: 1223 K**-150 MPa-10 min-**100K.min^{-1}**) allows achieving 94 % density. However due to high pressure, a composite graphite die is required. Finally, Figure 8 exhibits the three combined parameters (**Cycle C: 1223 K**-150 MPa-from 2 to 10 min-**200K.min^{-1}**). It clearly allows reaching high relative densities even for time as short as 2 minutes. Finally, cycle **A** (**1223 K**-100 MPa-10 min-**200K.min^{-1}**) has been used on the commercial powder and a density of 94 % has been achieved showing that these results are not only related to the very small size of the synthesized powders.

As the aim is to reach nanostructured dense ceramics, the grain size of the different samples has been studied by measuring the grain size on SEM micrographs (figure 9) and estimating the size of coherent domain by applying the Scherrer formulae to the (101) peaks of the XRD patterns (figure 10). Figure 9 clearly shows that the samples are composed by grains smaller than 100 nm. Figure 10 shows that the value obtained from the Scherrer formulae is consistent with the median grain size measured from SEM micrographs. Moreover, as the density increases, the grain size increases. However, for the ceramics with the highest densities, the grain size is around 60-70 nm. Therefore, the dense ceramics obtained by SPS are nanostructured.

The Seebeck coefficient and electrical conductivity, from 330 to 1000 K, of the sample sintered at **1223 K**-150 MPa-5 min-**200K.min^{-1}** are displayed in figure 11 a). The Seebeck coefficient shows a negative value which is consistent with the expected n-type conduction [2]. It improves from -234 to -290 $\mu V.K^{-1}$ at 330 and 855 K, respectively. For higher temperatures, the absolute value slightly reduces. This is 30 % higher than the -195 $\mu V.K^{-1}$ value measured by Vo et al. [16] at room temperature. The electrical conductivity increases on the whole temperature range which is characteristic of a semiconducting-like behaviour, from 550 to 1005 $S.m^{-1}$, at 330 and 1000 K, respectively. This is twice the value measured by Vo et al. [16]. The sample presents an unusual interesting feature: indeed, usually in semiconductors, when the electrical conductivity increases, the Seebeck coefficient decreases [25, 30, 43]. Similar behaviour can be observed in other compounds such as $Ca_3Co_4O_9$ or delafossites [27, 44]. However, the origin of this behaviour in SnO_2 remains unknown. Therefore, the power factor ($PF = S^2\sigma$) increases when temperature increases from 2.95×10^{-5} $W.m^{-1}.K^{-2}$ at 330 K to 7.75×10^{-5} $W.m^{-1}.K^{-2}$ at 1000 K (figure 11 b)). This value at 1000 K is similar to the one reported by Yanagiya et al. [15]. Temperature dependence of the

thermal conductivity (κ) from 373 to 1000 K is shown in figure 11 c). The thermal conductivity of the SnO_2 sample decreases when temperature increases from 6.59 $W.m^{-1}.K^{-1}$ at 373 K to 3.99 $W.m^{-1}.K^{-1}$ at 1000 K. These values can be compared to those reported for single crystals at room temperature that are 98 $W.m^{-1}.K^{-1}$ when parallel to the c-axis and 55 $W.m^{-1}.K^{-1}$ when perpendicular to c-axis [45] or in polycrystalline samples with micrometer-sized grains : between 25 to 40 $W.m^{-1}.K^{-1}$ at room temperature for grains from 2.5 to 8 µm, and around 10 $W.m^{-1}.K^{-1}$ at 1000 K [46]. This clearly demonstrates the ability of nanostructuring to significantly lower the thermal conductivity in oxides. Moreover, these values are slightly lower than the one recently reported in nanostructured Al-doped ZnO [47]. Figure 11 d) exhibits the temperature dependence of the thermoelectric figure of merit ZT (= PF/κ): it increases when temperature increases and reach 0.02 at 1000 K.

4. CONCLUSION

The spark plasma sintering behaviour of pure SnO_2 has been studied. It has demonstrated that it is not possible to work above **1223 K** to sinter pure SnO_2 by SPS. Indeed, at **1248 K**, SnO appears whereas at higher temperatures samples are composed by SnO_2 and metal Sn. The influence of each parameters (pressure, duration of the high temperature dwell and heating/cooling rate) has been studied. Three different cycles have been developed that allow achieving high relative densities (≥ 94 %): one of them allows to use conventional graphite die (**1223 K**-100 MPa-10 min-**200K.min^{-1}**) whereas the two others request the use of a high strength composite graphite die (**1223 K**-150 MPa-10 min-**100K.min^{-1}** and **1223 K**-150 MPa-from 2 to 10 min-**200K.min^{-1}**).

The study of the grain size shows that when the density increases the grain size increases to reach 60-70 nm for the high density samples. Therefore, SPS can be successfully used to

produce dense nanostructured SnO_2 ceramics without any sintering agent. The transport properties of the dense ceramics are the best reported for undoped SnO_2. This is the first step to allow studies of electrical properties of doped SnO_2 ceramics without the uncontrolled influence of the sintering agents. Moreover, nanostructuring is very efficient to lower thermal conductivity as values as low as 6.59 and 3.99 $W.m^{-1}.K^{-1}$ at 373 and 1000 K respectively, are measured in SPS nanostructured ceramics.

Acknowledgments

The authors acknowledge ADEME (Agence De l'Environnement et de la Maîtrise de l'Energie) for the financial support. The authors are grateful to use the SPS platform of Ile-de-France (France) and would like to thank B. Villeroy (ICMPE-CNRS, France) for his technical expertise. **The authors acknowledge the technical assistance of P.Y. Raynal from the plateforme des microscopies (microscopy center of University of Tours) for SEM images.**

REFERENCES

[1] G. J. McCarthy, J. M. Welton, X-Ray diffraction data for SnO_2. An illustration of the new powder data evaluation methods, Powder Diffraction 4 (1989) 156-159.

[2] Z. Chen, D. Pan, Z. Li, Z. Jiao, M. Wu, C.-H. Shek, C. M. L. Wu, J. K. L. Lai, Recent advances in tin dioxide materials: some developments in thin films, nanowires, and nanorods, Chemical Reviews 114 (2014) 7442-7486.

[3] M. Batzill, U. Diebold, The surface and materials science of tin oxide, Progress in Surface Science 79 (2005) 47-154.

[4] C. Kilic, A. Zunger, Origins of coexistence of conductivity and transparency in SnO_2, Phys. Rev. Lett. 88 (2002) 95501.

[5] A.K. Singh, A. Janotti, M. Scheffler, C.G. Van de Walle, Sources of electrical conductivity in SnO_2, Phys. Rev. Lett. 101 (2008) 55502.

[6] N. Yamazoe, New approaches for improving semiconductor gas sensors, Sens. Actuators B Chem. 5 (1991) 7-19.

[7] W. Göpel, K.D. Schierbaum, SnO_2 sensors: current status and future prospects, Sens. Actuators B Chem. 26 (1995) 1-12.

[8] E. Comini, Metal oxide nano-crystals for gas sensing, Anal. Chim. Acta 568 (2006) 28-40.

[9] T. Brousse, R. Retoux, U. Herterich, D.M. Schleich, Thin-Film Crystalline SnO_2-Lithium Electrodes, J. Electrochem. Soc. 145 (1998) 1-4.

[10] M. Miyauchi, A. Nakajima, T. Watanabe, K. Hashimoto, Photocatalysis and photoinduced hydrophilicity of various metal oxide thin films, Chem. Mater. 14 (2002) 2812-2816.

[11] F. Gu, S.F. Wang, M.K. Lü, G.J. Zhou, D. Xu, D.R. Yuan, Photoluminescence properties of SnO_2 nanoparticles synthesized by sol–gel method, J. Phys. Chem. B. 108 (2004) 8119-8123.

[12] S.A. Pianaro, P.R. Bueno, E. Longo, J.A. Varela, A new SnO_2-based varistor system, Journal of Materials Science Letters (1995) 692-694.

[13] A.B. Glot, R. Bulpett, A.I. Ivon, P.M. Gallegos-Acevedo, Electrical properties of SnO_2 ceramics for low voltage varistors, Phys. B Condens. Matter 457 (2015) 108-112.

[14] T. Tsubota, T. Ohno, N. Shiraishi, Y. Miyazaki, Thermoelectric properties of $Sn_{1-x-y}Ti_ySb_xO_2$ ceramics, Journal of Alloys and Compounds 463 (2008) 288-293.

[15] S. Yanagiya, N.V. Nong, J. Xu, M. Sonne, N. Pryds, Thermoelectric properties of SnO_2 ceramics doped with Sb and Zn, Journal of Electronic Materials 40 (2011) 674-677.

[16] T.T.X. Vo, T.N.H. Le, Q.N. Pham, C. Byl, D. Dragoe, M.-G. Barthés-Labrousse, D. Bérardan, N. Dragoe, Preparation and study of the thermoelectric properties of nanocrystalline $Sn_{1-x}Ta_xO_2$ ($0 \leq x \leq 0.04$), Phys. Status Solidi A 212 (2015) 2776-2784.

[17] X. Mao, R. Zhou, S. Zhang, L. Ding, L. Wan, S. Qin, Z. Chen, J. Xu, S. Miao, High efficiency dye-sensitized solar cells constructed with composites of TiO_2 and the hot-bubbling synthesized ultra-small SnO_2 nanocrystals, Sci. Rep. 6 (2016) 19390.

[18] T. Kimura, S. Inada, T. Yamaguchi, Microstructure development in SnO_2 with and without additives, Journal of Materials Science 24 (1989) 220-226.

[19] N. Dolet, J-M. Heintz, M. Onillon, J-P. Bonnet, Densification of 0.99 SnO_2-0.01 CuO mixture : Evidence for liquid phase sintering, Journal of the European Ceramic Society 9 (1992) 19-25.

[20] J.A. Varela, O.J. Whittemore, E. Longo, Pore size evolution during sintering of ceramic oxides, Ceramics International 16 (1990) 177-189.

[21] S. Zuca, M. Terzi, M. Zaharescu, K. Matisovsky, Contribution to the study of SnO_2-based ceramics. Part II Effect of various oxide additives on the sintering capacity and electrical conductivity of SnO_2, Journal of Materials Science 26 (1991) 1673-1676.

[22] J.A.Cerri, E.R. Leite, D. Gouvea, E. Longo, J.A. Varela, Effect of Cobalt(II) oxide and Manganese(IV) oxide on the sintering of tin(IV) oxide, J. Am. Ceram. Soc. 79 (1996) 799-804.

[23] M.S. Castro, C.M. Aldao, Characterization of SnO_2-varistors with different additives, Journal of the European Ceramic Society 18 (1998) 2233-2239.

[24] J. Lalande, R. Ollitrault-Fichet, P. Boch, Sintering behaviour of CuO-doped SnO_2, Journal of the European Ceramic Society 20 (2000) 2415-2420.

[25] E. Guilmeau, D. Berardan, C. Simon, A. Maignan, B. Raveau, D. Ovono Ovono, F. Delorme, Tuning the transport and thermoelectric properties of In_2O_3 bulk ceramics through doping at In-site, Journal of Applied Physics 106 (2009) 053715.

[26] S.J. Park, K. Hirota, H. Yamamura, Densification of nonadditive SnO_2 by hot isostatic pressing, Ceramics International. 10 (1984) 116.

[27] F. Delorme, C.F. Martin, P. Marudhachalam, D. Ovono Ovono, G. Guzman, Effect of Ca substitution by Sr on the thermoelectric properties of $Ca_3Co_4O_9$ ceramics, Journal of Alloys and Compounds 509 (2011) 2311-2315.

[28] S. Imine, F. Schoenstein, S. Mercone, M. Zaghrioui, N. Bettahar, N. Jouini, Bottom-up and new compaction processes: A way to tunable properties of nanostructured cobalt ferrite ceramics, Journal of the European Ceramic Society 31 (2011) 2943-2955.

[29] M. Bah , F. Giovannelli, F. Schoenstein, G. Feuillard, E. Le Clezio, I. Monot-Laffez, High electromechanical performance with spark plasma sintering of undoped $K_{0.5}Na_{0.5}NbO_3$ ceramics, Ceramics International 40 (2014) 7473-7480.

[30] P. Diaz-Chao, F. Giovannelli, O. Lebedev, D. Chateigner, L. Lutterotti, F. Delorme, E. Guilmeau, Textured Al-doped ZnO ceramics with isotropic grains, Journal of the European Ceramic Society, 2014, 34, 4247-4256.

[31] O. Guillon, J. Gonzalez-Julian, B. Dargatz, T. Kessel, G. Schierning, J. Raethel, M. Herrmann, Field-assisted sintering technology/spark plasma sintering: mechanisms, materials, and technology developments, Advanced Engineering Materials 16 (2014) 830-849.

[32] Y. Beynet, A. Izoulet, S. Guillemet-Fritsch, G. Chevallier, V. Bley, T. Pérel,F. Malpiece, J. Morel, C. Estournès, ZnO-based varistors prepared by spark plasma sintering, Journal of the European Ceramic Society 35 (2015) 1199-1208.

[33] F. Delorme, M. Bah, F. Schoenstein, F. Jean, M.Z. Jabli, I. Monot-Laffez, F. Giovannelli, Thermoelectric properties of oxygen deficient $(K_{0.5}Na_{0.5})NbO_3$ ceramics, Materials Letters 162 (2016) 24-27.

[34] E. Tõldsepp, F. Schoenstein. M. Amamra. R. Saar, E. Feldbach, A. Kanaev, M. Kirm, Spark plasma sintering of ultra-porous γ-Al_2O_3, Ceramics International 42 (2016) 11709-11715.

[35] F. Delorme, C. Chen, B. Pignon, F. Schoenstein, L. Perriere, F. Giovannelli, Promising high temperature thermoelectric properties of dense $Ba_2Co_9O_{14}$ ceramics, Journal of the European Ceramic Society 37 (2017) 2615-2620.

[36] W-J. Park, J. Wook, D-Y. Kim, Enhanced densification of pure SnO_2 by spark plasma sintering, Journal of Materials Science 40 (2005) 3825-3827.

[37] Q. Li, D. Zhnang, G. Luo, C. Li, Q. Shen, L. Zhang, Spark plasma sintering of undoped SnO_2 ceramics, Journal of Wuhan University of Technology-Mater. Sci. Ed. 26 (2011) 315-318.

[38] R. Dujardin, F. Delorme, B. Pintault, P. Belleville, C. Autret, I. Monot-Laffez, F. Giovannelli, A high yield one-pot aqueous synthesis of SnO_2 nanoparticles, Materials Letters 187 (2017) 151-153.

[39] S. Meir, S. Kalabukhov, N. Froumin, M.P. Dariel, N. Frage, Synthesis and densification of transparent magnesium aluminate spinel by SPS processing, J. Am. Ceram. Soc. 92 (2009) 358-364.

[40] K. Morita, B-N. Kim, H. Yoshida, K. Hiraga, Y. Sakka, Distribution of carbon contamination in $MgAl_2O_4$ spinel occurring during spark-plasma-sintering (SPS) processing: I - Effect of heating rate and post-annealing, Journal of the European Ceramic Society 37 (2018) 2588-2595.

[41] E.A. Olevsky, S. Kandukuri, L. Froyen, Consolidation enhancement in spark-plasma sintering: Impact of high heating rates, Journal of Applied Physics 102 (2007) 114913.

[42] W. Luo, J. Pan, Effects of surface diffusion and heating rate on first-stage sintering that densifies by grain-boundary diffusion, J. Am. Ceram. Soc. 98 (2015) 3483-3489.

[43] A. Shakouri, Recent developments in semiconductor thermoelectric physics and materials, Annu. Rev. Mater. Res. 41 (2011) 399-431.

[44] K. Koumoto, H. Koduka, W-S. Seo, Thermoelectric properties of single crystal $CuAlO_2$ with a layered structure, Journal of Materials Chemistry 11 (2001) 251-252.

[45] P. Turkes, C. Pluntke C., R. Helbig, Thermal conductivity of SnO_2 single crystals, J. Phys. C: Solid St. Phys. 13 (1980) 4941-4951.

[46] S. Fayette, D.S. Smith, A. Smith, C. Matin, Influence of grain size on the thermal conductivity of tin oxide ceramics, Journal of the European Ceramic Society 20 (2000) 297-302.

[47] F. Giovannelli, C. Chen, P. Díaz-Chao, E. Guilmeau, F. Delorme, Thermal conductivity and stability of Al-doped ZnO nanostructured ceramics, Journal of the European Ceramic Society 38 (2018) 5015-5020.

FIGURE CAPTION

Table 1: Sintering parameters of the three cycles achieving high relative density.

Figure 1: a) SEM image of the particles of the Aldrich SnO_2 precursor, b) TEM image of the SnO_2 nanoparticles obtained according to the process described by Dujardin et al. [38].

Figure 2: Image of Sn beads appearing on the top of the graphite die after the SPS cycle.

Figure 3: XRD pattern of the pellet sintered at a) **1323 K** under a pressure of 37.5 MPa during 5 minutes (heating and cooling rate of **100K.min^{-1}**), b) **1248 K**-100MPa-5min (heating and cooling rate of **100K.min^{-1}**), c) **1223 K**-100MPa-5min (heating and cooling rate of **100K.min^{-1}**).

Figure 4: SEM image of the microstructure of the pellet sintered at **1223 K**, under 100 MPa during 5 minutes.

Figure 5: Relative density versus duration of the high temperature dwell of the SPS cycle (**1223 K**-100 MPa-**100K.min^{-1}**).

Figure 6: Relative density versus applied pressure during the SPS cycle (**1223 K**-5 min-**100K.min^{-1}**).

Figure 7: Relative density versus heating/cooling rate (**1223 K**-100 MPa-5 min).

Figure 8: Relative density versus duration of the high temperature dwell of the SPS cycle (**1223 K**-150 MPa-**200K.min^{-1}**).

Figure 9: SEM micrograph of the sample sintered at **1223 K**-150 MPa-2 min-**200K.min^{-1}**.

Figure 10: Comparison of the grain size of the different samples obtained by SEM measurements and from the Scherrer formulae.

Figure 11: Temperature dependence of a) the Seebeck coefficient and the electrical conductivity, b) the power factor, c) the thermal conductivity, d) the figure of merit, **of the sample sintered with cycle A (1223K-150 MPa-5 min-200K.min^{-1}).**

Cycle	Maximum Temperature (K)	Applied Pressure (Mpa)	Dwell Duration (min)	Heating/Cooling Rates ($K.min^{-1}$)	Die	Relative Density (%)
A	1223	100	10	200	Conventional Graphite	95
B	1223	150	10	100	Composite Graphite	94
C	1223	150	from 2 to 10	200	Composite Graphite	from 94 to 96

Table 1

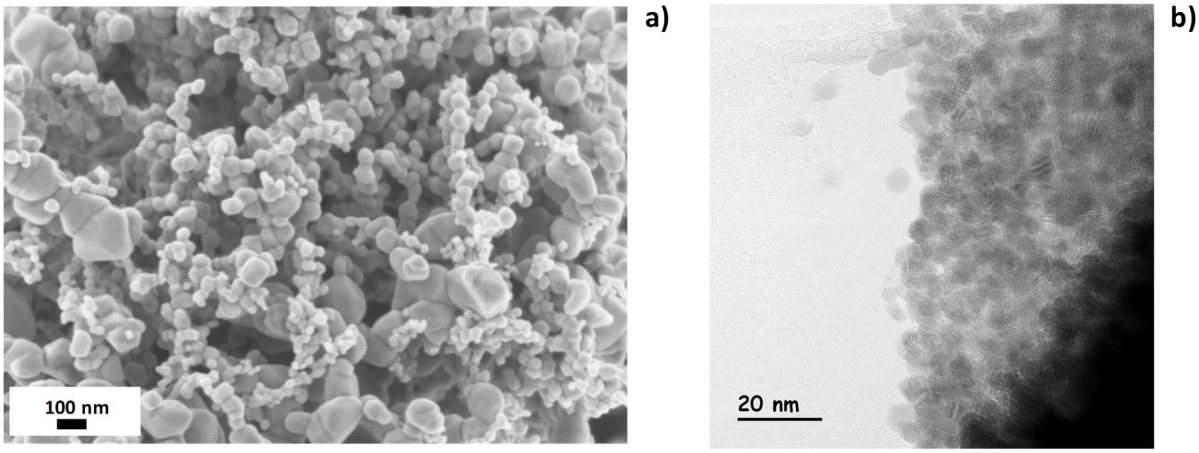

Figure 1

Figure 2

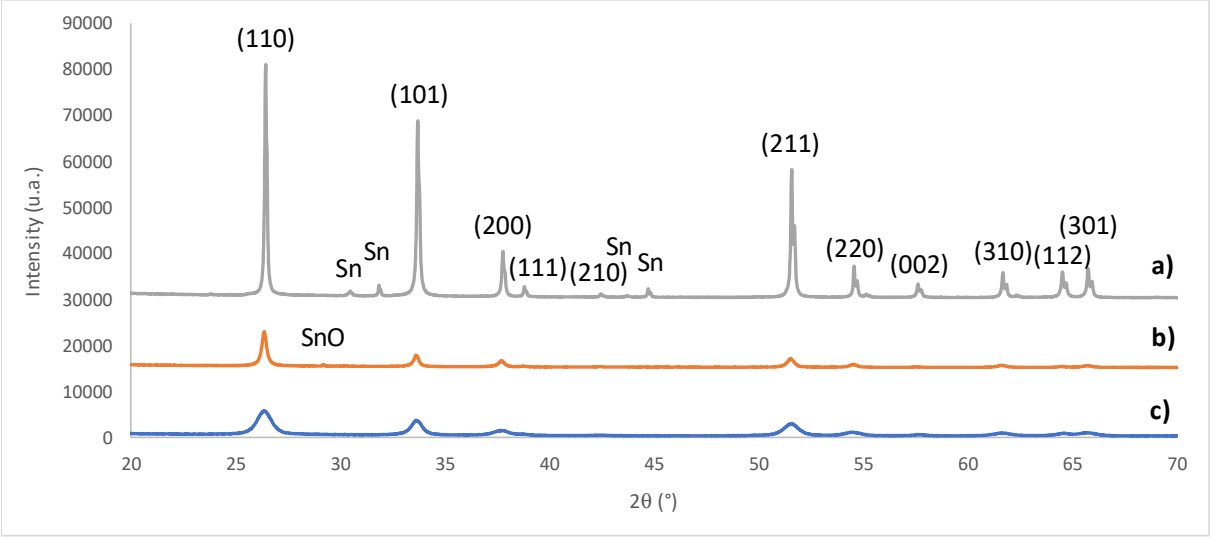
90000
80000
70000
60000
50000
40000
30000
20000
10000
0
Intensity (u.a.)
(110)
(101)
(200)
(211)
(220)
(002)
(310)
(112)
(301)
(111)
(210)
Sn
Sn
Sn
Sn
SnO
a)
b)
c)
20
25
30
35
40
45
50
55
60
65
70
2θ (°)

Figure 3

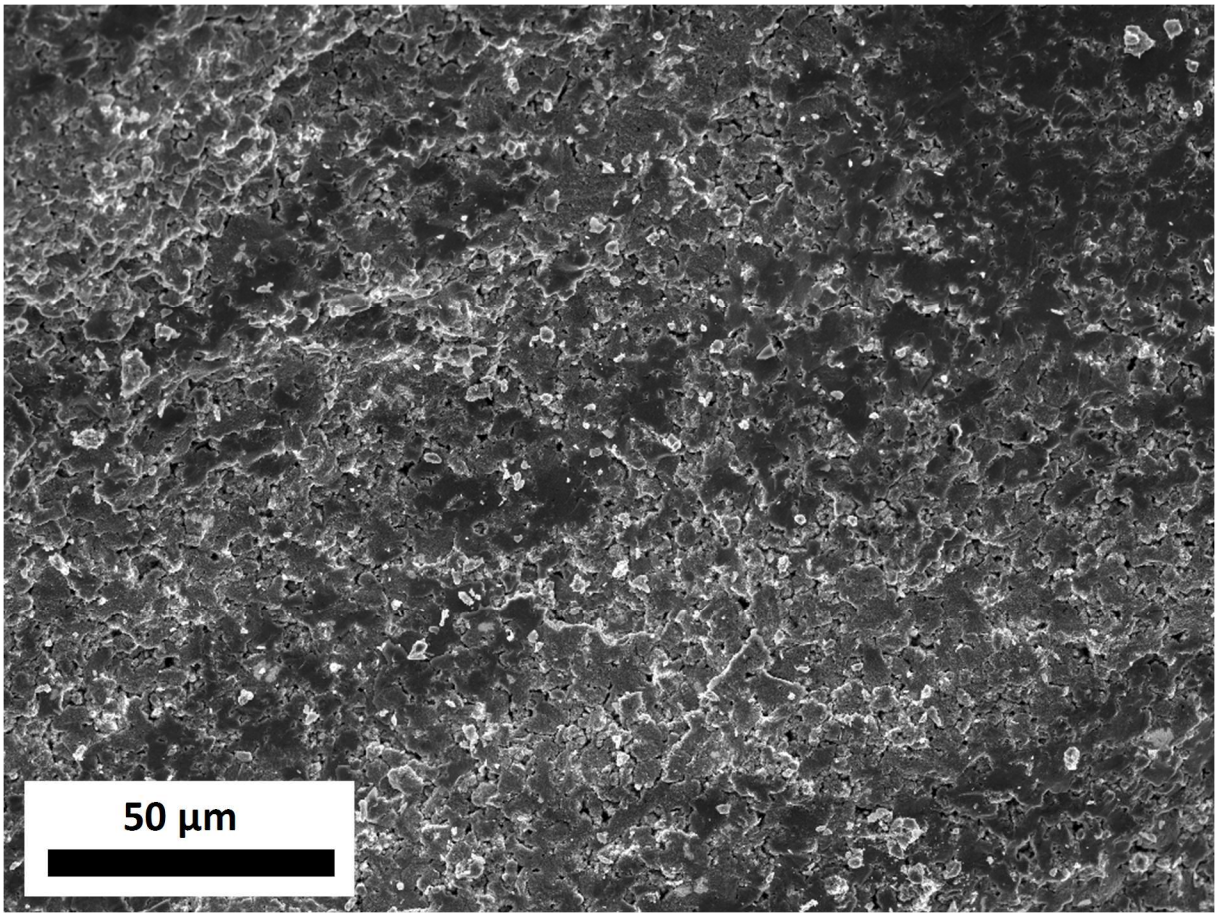

Figure 4

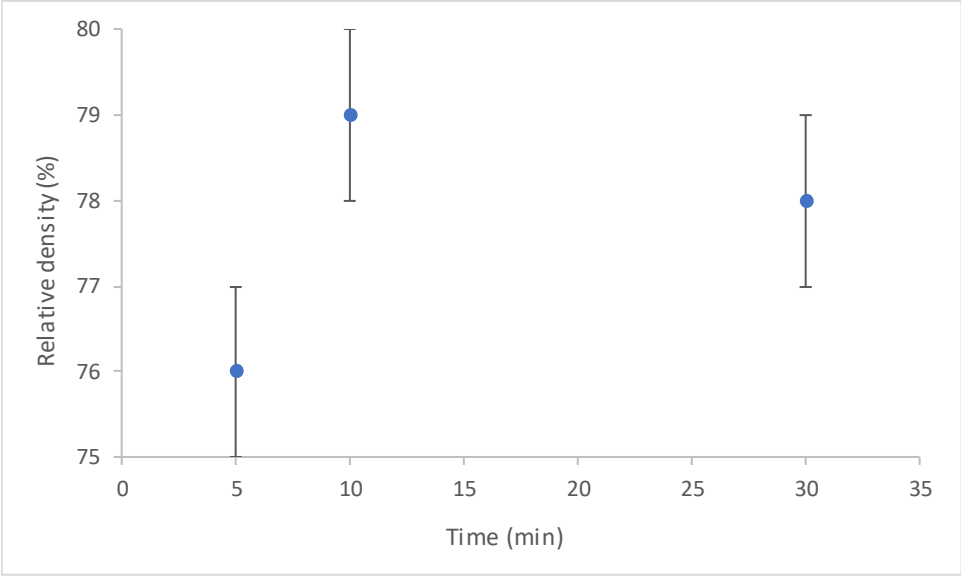

Figure 5

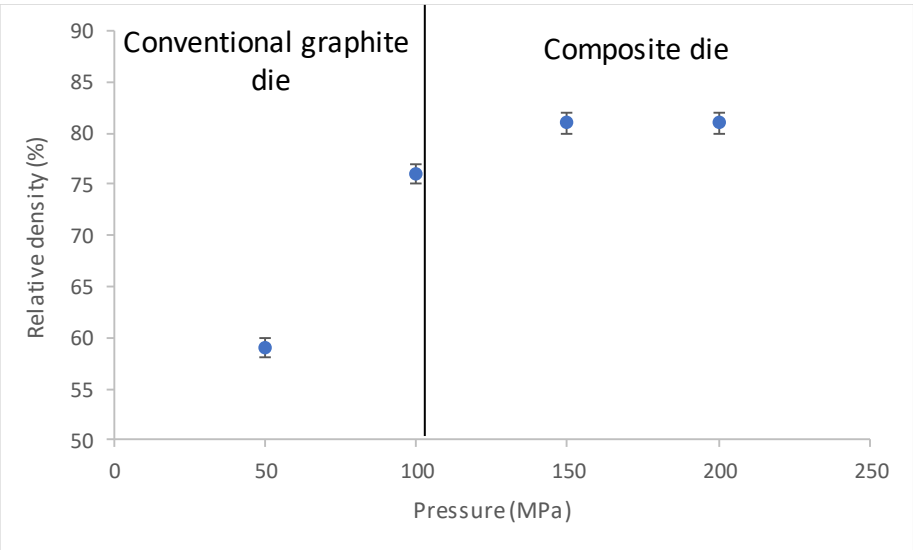
Conventional graphite die
Composite die
Relative density (%)
90
85
80
75
70
65
60
55
50
0
50
100
150
200
250
Pressure (MPa)

Figure 6

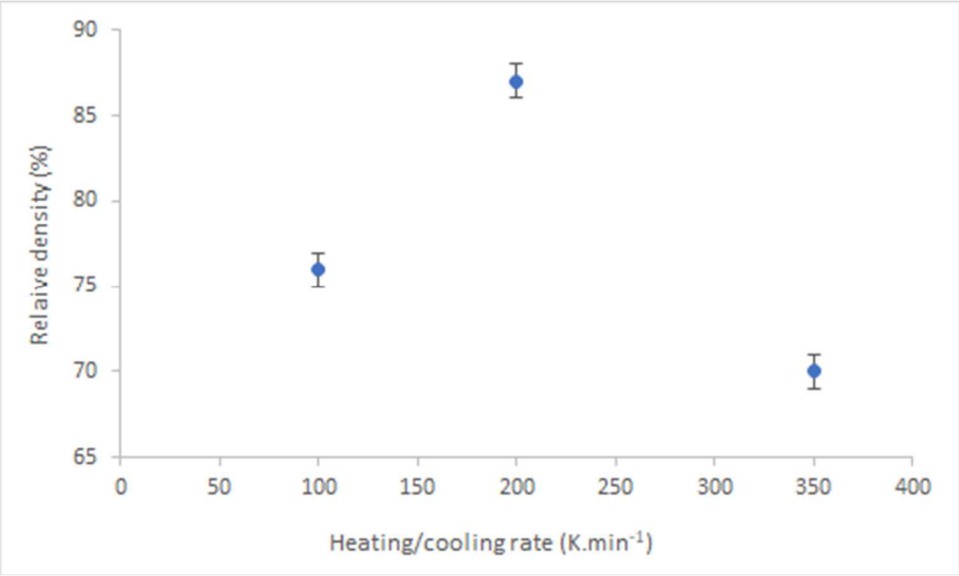
90
85
80
75
70
65
Relaive density (%)
0
50
100
150
200
250
300
350
400
Heating/cooling rate (K.min-1)

Figure 7

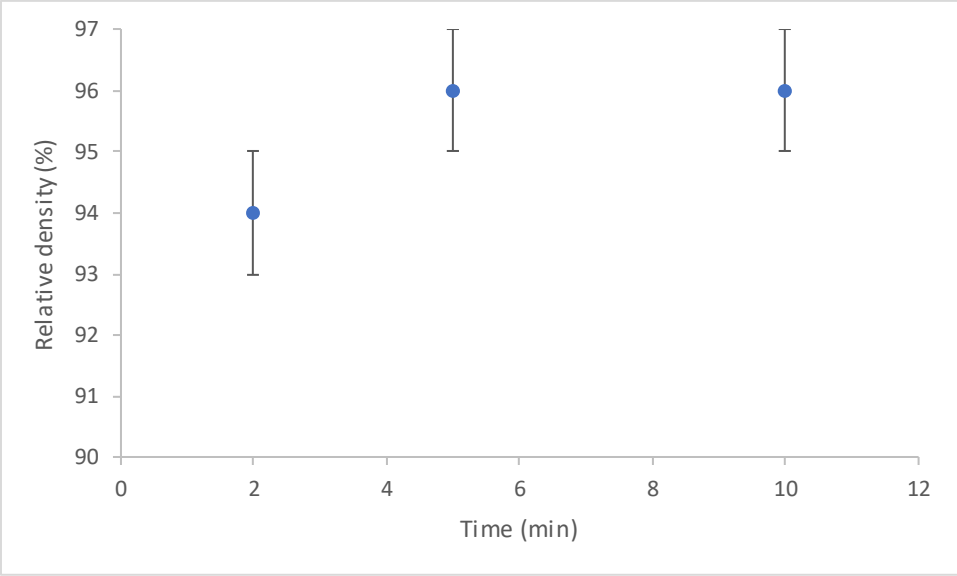

Figure 8

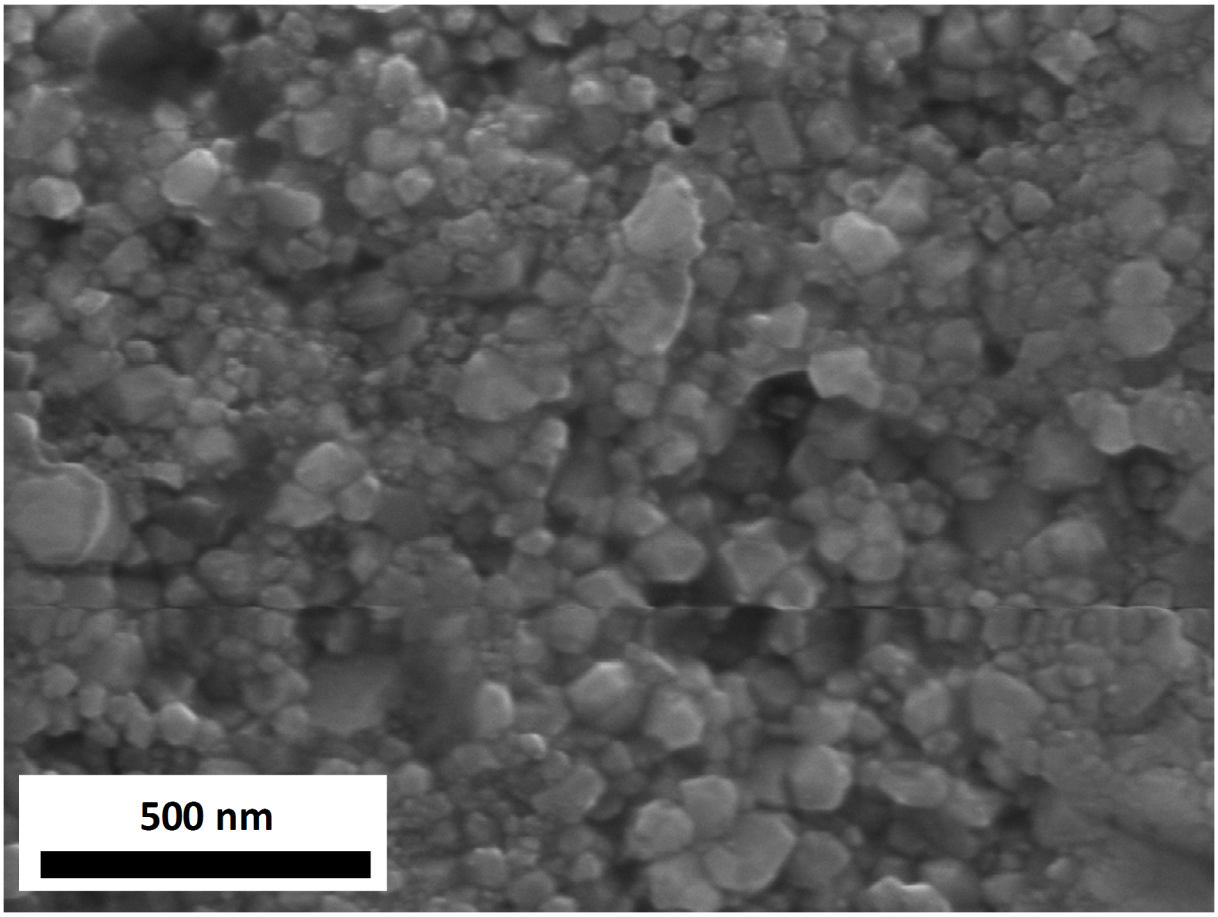

Figure 9

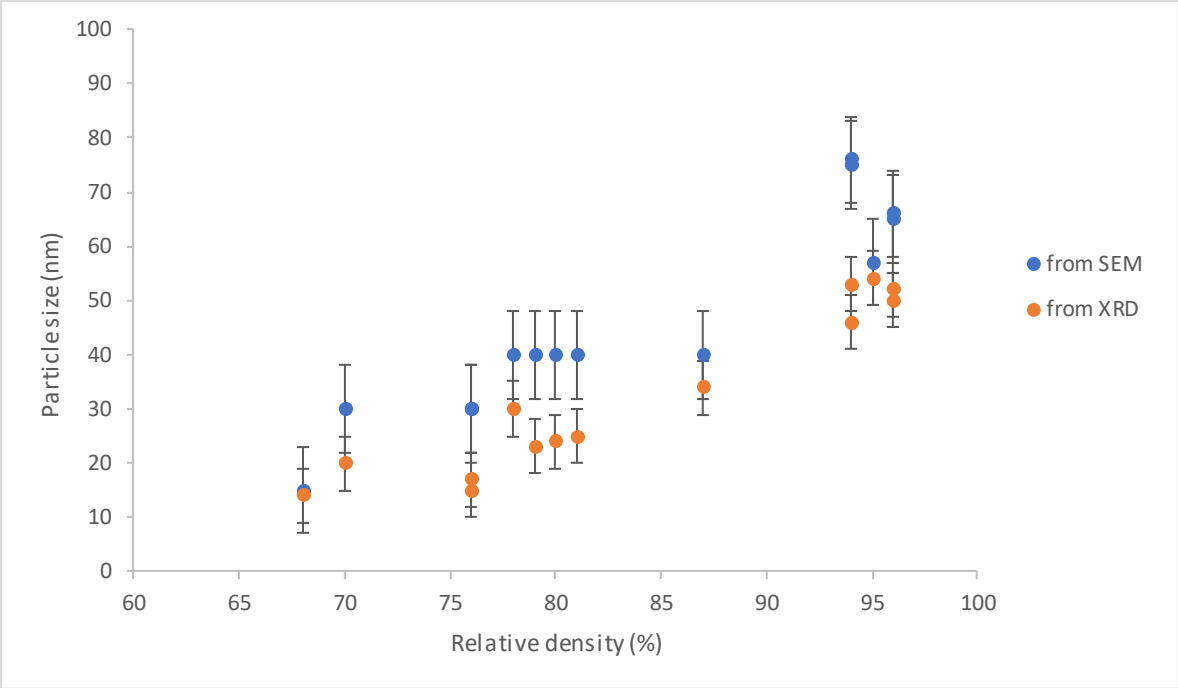
100
90
80
70
60
50
40
30
20
10
0
Particle size (nm)
60
65
70
75
80
85
90
95
100
Relative density (%)
from SEM
from XRD

Figure 10

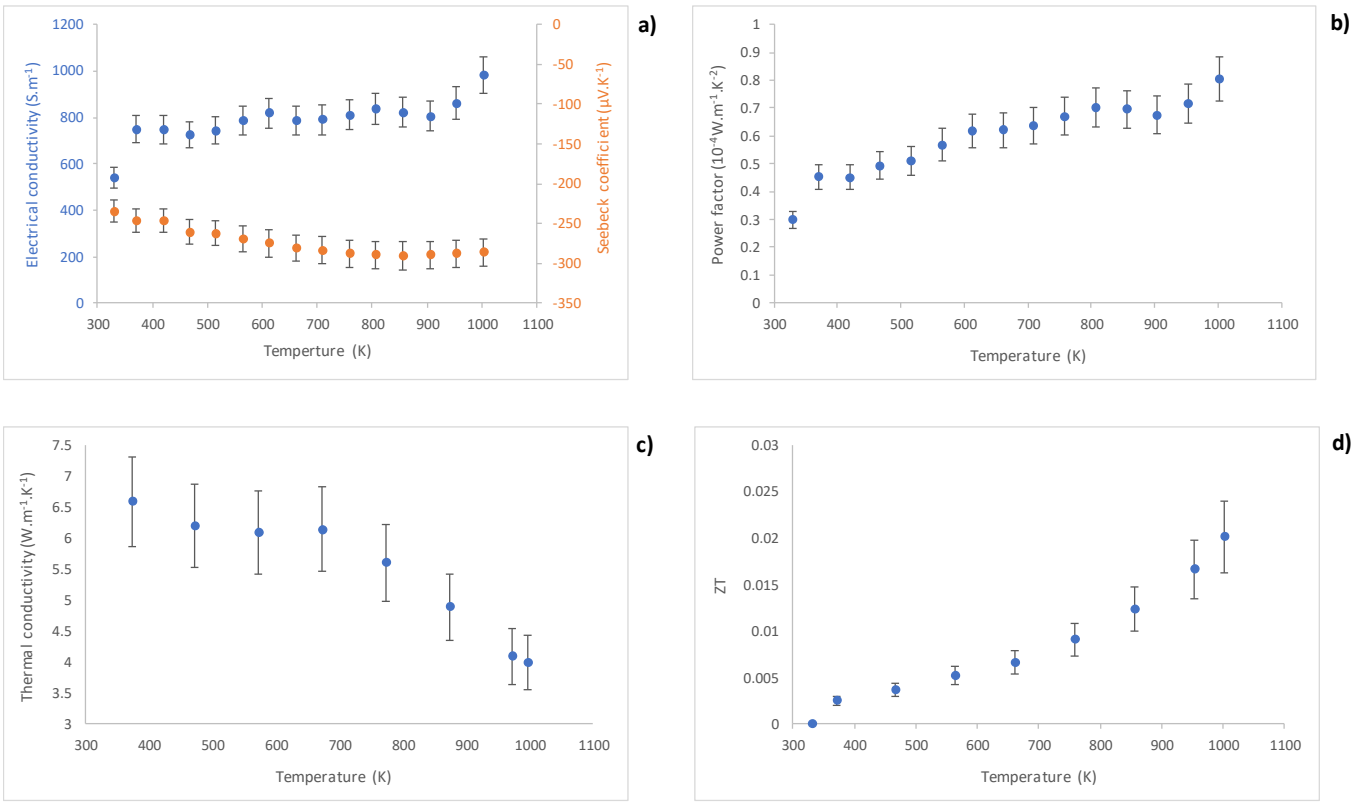
a)
Electrical conductivity (S.m-1)
Seebeck coefficient (µV.K-1)
Temperture (K)
b)
Power factor (10-4W.m-1.K-2)
Temperature (K)
c)
Thermal conductivity (W.m-1.K-1)
Temperature (K)
d)
ZT
Temperature (K)

Figure 11